Electrically tunable plasmomechanical oscillators for localized modulation, transduction, and amplification

Brian J. Roxworthy[1,*] and Vladimir A. Aksyuk[1]

[1]*Center for Nanoscale Science and Technology, National Institute of Standards and Technology, Gaithersburg, MD 20899, USA*

[*]*Corresponding author: brian.roxworthy@nist.gov*

Plasmomechanical systems are an emerging class of device that hold great promise for manipulating light-matter interactions with high speed and sub-diffraction spatial resolution. However, realizing their potential requires developing active plasmomechanical systems that can localize their functionality to the level of an individual sub-wavelength plasmonic resonator. Here, we present an active, electrically tunable plasmomechanical system that uses a localized-gap plasmonic resonator to mediate optical, thermal, and mechanical interactions within a subwavelength footprint. Our device enables facile electromechanical modulation of localized plasmons, selective sub-diffraction transduction of nanomechanical motion, and functions as a plasmomechanical oscillator that can be injection locked to and thus amplify weak external stimuli. These functionalities benefit applications in nanomechanical sensing, spatial light modulators, and reconfigurable metasurfaces.

Introduction

Controlling the interaction of light with matter leads to fundamental advances and fosters technological breakthroughs in many fields [1]. Plasmonic systems are particularly attractive for manipulating these interactions – they enable extreme confinement of optical wavelengths λ, producing mode volumes that can be thousands of times smaller than λ^3. Sub-diffraction localization both enhances light-matter interactions and renders plasmonic modes highly sensitive to their local environment. As a consequence, plasmonic devices have driven advances in diverse areas including nanoscale laser sources [2], bio-chemical detection [3], particle trapping and manipulation [4,5], energy harvesting [6], nonlinear optics [7], and quantum devices [8]. Nevertheless, realizing the full potential of plasmonics requires platforms that allow flexible and reversible tuning of localized modes. A new class of plasmomechanical systems, which introduce mechanical freedom into otherwise static structures, is emerging in response to this demand for more versatile control of light-matter interaction and greater device functionality [9–13].

Plasmomechanical devices introduce mechanical freedom into otherwise static plasmonic structures. When two plasmonic structures ("meta-atoms") are brought in close proximity, their surface plasmons interact and hybridize [14]. Hybridization lowers the energy of the fundamental localized mode, analogous to atomic orbitals, inducing a strongly gap-dependent frequency shift in the resulting plasmonic resonator; sometimes referred to as a "metamolecule" [15]. As a result of tight energy confinement and gap-dependent hybridization, plasmomechanical devices can generate extremely large resonance frequency shifts for small displacements, viz. large optomechanical coupling constants. Furthermore, the localization phenomenon is fundamentally linked with optical losses [16], which together enables plasmonic resonators to function as nanoscale heat sources. Combining plasmomechanics with an actuation scheme opens the possibility to strongly localize, enhance, and tune interactions between distinct physical domains – optical, mechanical, thermal, acoustic, and more [17]. The importance of plasmomechanical systems thus lies not only in their technological relevance, for example, to randomly addressable metasurfaces and high-spatial-resolution spatial light modulators [17], but also in their potential for studying optomechanics at unprecedented small length scales, potentially leading to new fundamental advances in transduction, amplification, and modulation. Accessing these possibilities requires creation of plasmomechanical systems that are tunable at the level

of individual, nanometer-sized structures. However, this ability is challenging to realize in existing systems.

In this article, we introduce a new active plasmomechanical system based on electrically tunable localized-gap plasmon resonators (LGPRs), which can effectively localize and control the interactions between optical, thermal, and mechanical degrees of freedom within a subwavelength footprint. Specifically, we use electrostatic actuation to drive the mechanics, engaging large optomechanical coupling constants to attain both high-contrast modulation of individual LGP resonances and, inversely, localized plasmonic transduction of nanomechanical motion. Absorption from the LGPR locally couples the optics and mechanics to the thermal modes of the system. Making use of bimorph actuation, we demonstrate that this thermo-mechanical coupling can induce self-oscillation of a nanomechanical device, forming a plasmomechanical oscillator (PMO). Finally, we show that the PMO, whose dynamics are analogous to radiation pressure-driven optomechanical oscillators [18,19], can be injection-locked to a small-amplitude mechanical stimulus. This feature allows the PMO to function as a high-bandwidth amplifier of mechanically addressable perturbations with *a priori* unknown frequency.

Device concept and design

Our active plasmomechanical system is obtained by embedding a point-like LGPR into a fully-functional nano-electro-mechanical system (NEMS) capable of electrostatic and thermal actuation [20]. The shape and the gap size of a given LGPR defines its resonances (optical modes) and their corresponding frequencies, intrinsic losses and radiation coupling rates. While the LGPRs support multiple optical modes, their energies are widely separated and only a single mode will be relevant for each of the described experiments. The functionality of the plasmomechanical system derives from localized coupling of these optical modes to mechanical motion, which is engaged via electrical actuation, changing both the optical frequency and the radiation coupling rate. Additionally, plasmonic losses convert optical energy into heat, and thus provide dynamic thermal excitation to the NEMS *via* thermo-mechanical coupling.

The mechanical and thermal responses of the NEMS can each be described by their modes. The static deformation and dynamic mechanical motion can be represented as a superposition of mechanical modes, whose shapes, resonance frequencies, damping, and stiffness all depend on the NEMS geometry and materials. Similarly, the time-dependent temperature distribution in the structure can be described by thermal modes [21]. The thermal modes are driven by the heat generated from plasmonic absorption and have distinct geometry and material-dependent shapes and decay time constants. Differential thermal expansion of an engineered metal-dielectric bimorph structure produces thermo-mechanical coupling, allowing the thermal modes to drive the mechanical. Crucially, the point-like nature of the LGPR enables selective coupling with spatially-extended thermal and mechanical modes based on the resonator location. This feature, along with electrostatic actuation, can be used to electrically tune the LGP resonances, to selectively transduce mechanical modes, and to produce self-oscillations of the NEMS. We demonstrate this explicitly for the mechanical modes. We note that while accounting for only the fundamental thermal mode is sufficient to quantitatively describe our results, higher-order thermal modes may be engineered to play an important role in future systems [21,22].

For our plasmomechanical system, illustrated in Fig. 1a, we choose a simple cantilever design comprising a ≈ 165 nm SiNx thickness and a ≈ 15 nm gold layer on top, patterned separately to create the desired thermal bimorph shape. Each cantilever is suspended above an underlying stationary gold pad and can be electrostatically actuated by applying a voltage between the top gold layer and the pad. Multiple cantilevers, fashioned into arrays on a single wirebonded chip, are either ≈ 500 nm or ≈ 2 μm wide and

vary in length from ≈ 1.5 μm to ≈ 6 μm. A nanoscale, ≈ 40 nm thick gold cuboid is embedded in the cantilever's underside at varying positions along the length. The LGPR is defined by the embedded cuboid, the gold pad, and the gap (g) separating the two gold surfaces (Fig. 1a, inset). This gap, nominally 20 nm, increases quadratically along the cantilever length due to residual stress gradients from the fabrication process (Supplement 1, Section 1), which cause the cantilever to curl away from the pad, as seen in atomic force microscope (AFM) images and data (Fig. 1b, Supplement 1, Section 2). The placement of the LGPR relative to the cantilever base therefore determines its initial gap and thus the optomechanical behavior of each device.

The optical-frequency resonance of the LGPR can be understood by viewing it as a truncated metal-insulator-metal waveguide, wherein propagating gap plasmons confined to the narrow gap area are reflected from the edges of the top cuboid, forming a standing wave parallel to the gold surfaces with a round-trip phase of $2\pi\, m$ [23]. We utilize an $m = 3$ LGP mode, in order to enhance the plasmonic quality factor Q_{LGP} [10], by designing a cuboid nominally measuring (350×160×40) nm^3 in length, width, and height, respectively. The LGP mode manifests as a pronounced Lorentzian-shaped dip in the optical reflectance spectrum, $R(\lambda)$, centered at wavelength (frequency) λ_{LGP} ($\omega_{\mathrm{LGP}} = 2\pi c/\lambda_{\mathrm{LGP}}$, c being the vacuum speed of light) in the wavelength range from ≈ 760 nm to ≈ 820 nm. Similarly, an $m = 1$ mode can be produced in this wavelength range using a (90×75×40) nm^3 cuboid. The calculated $R(\lambda)$ curves in Fig. 2a (Supplement 1, Section 3) reveal that decreasing the initial gap from 50 nm to 10 nm causes a pronounced shift in λ_{LGP} toward longer wavelengths (lower frequencies). The constant $G_{\mathrm{om}} = \partial\omega_{\mathrm{LGP}}/\partial x$ (where the coordinate $x \equiv -g$) associated with this dispersive optomechanical coupling can reach remarkably large values up to $2\pi \cdot 7$ THz nm^{-1} at small gaps, but drops by more than an order of magnitude for $g > 35$ nm (Fig. 2b); the equivalent vacuum coupling rate is $g_0 = G_{\mathrm{om}} \cdot x_{\mathrm{zpf}} \approx 2\pi \cdot 225$ MHz, where $x_{\mathrm{zpf}} = \sqrt{\hbar\,(2\, m_{\mathrm{eff}}\, \omega_{\mathrm{m}})^{-1}} \approx 30$ fm is the amplitude of the zero-point fluctuation of the cantilever with effective mass m_{eff} and frequency ω_{m} at the LGPR location. Additionally, reactive optomechanical coupling, characterized by changes in the resonance coupling depth and Q_{LGP} with gap [24], is also present in our system. For gaps above 35 nm, the LGPR responds purely reactively, such that the absorbance $A \approx 1 - R$ obeys $\partial A/\partial x < 0$ for all wavelengths in the range considered. Based on the deflected cantilever shape determined from AFM data (Fig. 1b), the transition to purely reactive coupling is expected to occur for LGPRs placed greater than 1.5 μm from the base. The increase in coupling depth is a result of additional losses in the system occurring at larger gaps. In particular, incident radiation couples more strongly to the LGP mode resulting in larger absorptive losses, as well as larger scattering outside the collection NA. This continuum of reactive to dispersive coupling can be tuned by judicious LGPR placement, and is therefore useful for shaping the overall performance of our plasmomechanical system.

Electro-optic modulation by actuated plasmonic resonators

We make use of the large dispersive optomechanical coupling to demonstrate low-voltage, high-contrast modulation of incident light reflected from individual LGPRs. The modulation experiments, conducted with the apparatus shown in Fig. 3a, are performed in ambient air conditions. In this application, an applied voltage induces an electrostatic force that closes the gap and thereby modifies the LGP resonance. The voltage is switched at 2 Hz with a maximum amplitude of 0 V to 2.75 V. Application of larger voltages for an extended time leads to the cantilever coming into close mechanical contact with the pad over a large area, causing irreversible collapse of the device due to stiction. Figure 3b shows experimentally measured reflectance spectra for increasing applied voltages with a LGPR located ≈ 1.5 μm from the base of a ≈ 4 μm cantilever. These data are collected using a confocal spectroscopy setup with a broadband supercontinuum laser (Fig. 3a). The reflectance is measured by

first collecting a reference spectrum $B(\lambda)$ of the supercontinuum laser by placing the focused spot on the cantilever, displaced from the LGPR by ≈ 1 μm. Then, we focus on the LGPR and collect the spectrum $R_0(\lambda)$. The plotted reflectance is $R(\lambda)$= $R_0(\lambda)/B(\lambda)$. Optical power delivered to the LGPR is ≈ 2.5 mW in this experiment. The reference reflectance $B(\lambda)$ is indistinguishable from the bare gold pad reflectance within the LGPR wavelength range (Supplement 1, Section 6).

Continuous, voltage-controlled shifts in the LGP resonance are measured up to a maximum of $\delta\lambda_{\mathrm{LGP}}$ = (42 $\pm$ 1.8) nm from its original wavelength of λ_{LGP} = (763 $\pm$ 0.1) nm (Fig. 3c); uncertainties are derived from Lorentzian fits. Given the native linewidth $\Delta\lambda$ = (39 $\pm$ 0.5) nm, the relative shift is $\delta\lambda_{\mathrm{LGP}}/\Delta\lambda$ = 1.07 $\pm$ 0.05 (Fig. 3d). For a similar device having a LGPR closer to the cantilever base (≈ 0.5 μm), the same voltage induces a smaller motion and thus a smaller shift $\delta\lambda_{\mathrm{LGP}}/\Delta\lambda$ = 0.35 $\pm$ 0.04. Achieving $\delta\lambda_{\mathrm{LGP}}/\Delta\lambda$ > 1 at a CMOS (complementary metal-oxide semiconductor) compatible voltage of 2.75 V (Supplement 2) means that the phase of the light re-radiated into the far-field by the device is tuned by more than π rad, representing a technologically important milestone necessary for implementing efficient phase and high-contrast amplitude modulators. This LGPR optical modulator can be compared to other systems by deriving its effective electro-optical Kerr coefficient, given by $\mathcal{K} = \Delta\varphi \left(2\pi L_{\mathrm{opt}} \left|E_{\Delta\varphi}\right|^2\right)^{-1} \approx d_{\mathrm{V}}(4\,V_{\pi}^2)^{-1}$, where d_{V} is the effective electrical thickness of the cantilever with gap g ≈ 30 nm, thickness t_{cant} ≈ 165 nm, $L_{\mathrm{opt}} \approx 2\,d_{\mathrm{V}}$ is the optical thickness of the modulator, and $V_{\pi} = E_{\pi}\,d_{\mathrm{V}}$ is the applied voltage required to induce a phase shift of π rad [25]. Using experimentally measured parameters, we find $\mathcal{K} \approx 2 \times 10^{-8}$ m V^{-2}. This value is extremely large compared to natural Kerr materials and comparable to state-of-the art systems based on two-dimensional materials [26]. The large $\mathcal{K}$, in combination with the measured intensity modulation of up to 40 % (Fig. 3b, inset), shows that a single tunable LGPR can act as an effective far-field optical modulator, notwithstanding its sub-wavelength size.

The effectiveness of the modulator draws from the fact that the LGPR's mode has an optical cross section larger than its physical size, and that it can be tuned by more than its linewidth by only a few nanometers of mechanical motion. Nanoelectromechanical devices can induce such motion within tens of nanoseconds at low voltage, enabling high-speed switching. This modulation principle is applicable across a wide range of optical frequencies, from the visible into mid- and long-wavelength infrared. Despite intrinsic limitations imposed by plasmonic losses, such devices open interesting possibilities for electrically controlled optical switches, spatial light modulators, and fast-tunable metasurfaces, particularly in the longer-wavelength regimes.

Selective transduction by localized plasmomechanical coupling

The plasmomechanical coupling is localized to the sub-wavelength footprint of the LGPR, and its location within the mechanical structure can be chosen to selectively couple to various nanomechanical modes. The ability to distinguish between mode shapes represents a key advantage of plasmomechanical systems for transducing nanomechanical dynamics, yet it has not been demonstrated to date. We demonstrate selective transduction of the mechanical modes using two separate, 4 μm cantilevers (Fig. 4), with LGPRs placed at ≈ 0.5 μm (left panel) or ≈ 2.0 μm (right panel) from their base. A vector network analyzer supplies a weak ≈ 40 mV harmonic stimulus of varying frequency to each cantilever, while its motion is optomechanically read out with a wavelength-tunable probe laser focused on the LGPR. The optical power delivered to the LGPR is ≈ 2 mW in this experiment. An intrinsic DC voltage bias exists in our devices, allowing electrostatic AC driving of the devices (Supplement 1, Section 4). The normalized magnitudes (Fig. 4a) reveal that both devices have similar mechanical responses

characterized by a ≈ 10 MHz fundamental and a ≈ 55 MHz second-order flexural mode. However, for the LGPR at 0.5 μm, the second order mode dominates the response, whereas at 2.0 μm, transduction is dominated by the fundamental mode. The reversal of measured motion power from these devices under identical mechanical excitation clearly indicates that transduction occurs localized to the footprint of the point-like LGPR.

The LGPR location not only changes its coupling to the mechanical modes, but also changes the plasmonic gap – due to the upward curvature of the cantilever (Fig. 1b), the gap is larger farther from the base. This switches the optomechanical coupling regime from dispersive for the LGPR at 0.5 μm to reactive for the LGPR at 2 μm, as evident from simulated (Fig. 2a) and experimental (Fig. 3b) results, and qualitatively changes the dependence of the transduced signal on the probe laser wavelength. Figure 4 shows that for the 0.5 μm case, transduction vanishes for zero detuning relative to λ_{LGP} (gray data points) and the phase response (Fig. 4b, the phase delay between the harmonic excitation signal and the resulting optically-transduced harmonic mechanical response is measured with the network analyzer) experiences a π-phase shift as the laser is tuned through the LGP resonance. The transduction signal, proportional to $\partial R/\partial x$, changes sign with detuning, indicating dispersive optomechanical coupling [24,27]. In the 2.0 μm case, we observe a clear motion signal for any detuning, with the largest signal on resonance and no phase reversal. The detuning-independent phase responses and non-zero $\partial R/\partial x$ on resonance indicate that this LGPR is reactively coupled, responding primarily by changing its coupling rate to free-space radiation, with minimal wavelength shift.

The locality of the optomechanical interaction is particularly useful for motion readout of sub-wavelength nanomechanical structures. To demonstrate this capability, we further miniaturize the plasmomechanical system using even smaller (90×75×40) nm^3 LGPRs and 500 nm wide cantilevers. This LGPR size supports an $m = 1$ resonance with λ_{LGP} ≈ 760 nm, Q_{LGP} ≈ 10 and a deep modulation (Fig. 5c). Figures 5a and 5b show false-color scanning electron micrographs of 2 μm length (Fig. 5a) and 1.5 μm length (Fig. 5b) cantilevers. The normalized magnitudes of the LGPR frequency-dependent displacement responses to electrostatic actuation (measured with the network analyzer) show fundamental mechanical modes at ≈ 44 MHz and ≈ 66 MHz, which agree well with finite-element calculations. The motion signals appear only when the probe laser is focused directly on the LGPR, indicating that they derive from the sub-wavelength optomechanical interactions facilitated by LGPR (Supplement 1, Section 6).

The plasmomechanical oscillator

In systems where optical absorption is coupled to mechanical motion, a suitably engineered thermo-mechanical coupling is a well-studied mechanism for inducing damping, as well as mechanical line narrowing and regenerative mechanical oscillations [28–33]. We observe these effects in our plasmomechanical system using the bimorph actuator, which produces thermo-mechanical coupling from the heat produced by LGPR absorption and the thermal expansion mismatch between the top gold electrode and the silicon nitride cantilever. Thermo-mechanical coupling enriches our system's behavior, allowing an individual LGPR to induce optically powered self-oscillation of the NEMS – a plasmomechanical oscillator (PMO). This PMO is the smallest device of its type, and can be optically driven using a broad range of wavelengths. Further, localized plasmonic absorption creates large thermal gradients, opening interesting possibilities for engineered optical excitation of higher-order thermal modes of nanomechanical devices [21,22]. The non-uniform temperature distributions and faster relaxation times of these thermal modes can potentially facilitate selective dynamic coupling to high order mechanical modes.

To demonstrate the PMO, we place our devices in vacuum primarily to reduce the effects of squeeze-film damping from ambient air (Fig. 6a). We use a 6 μm long cantilever that has a fundamental mechanical mode frequency of ≈ 4 MHz, with a dispersively coupled LGPR located ≈ 0.5 μm from the base. Figure 6b shows motion spectra of the cantilever's fundamental mode, transduced by the LGPR with a blue-detuned laser; calibration is performed using equipartition at low laser power [34] (Supplement 1, section 5). The measured motion amplitude (Fig. 6c) increases gradually up to a pump power of approximately 1100 μW, beyond which a sharp transition occurs, whereby the amplitude increases by more than 50 dB and saturates at high power. Associated with this transition is a reduction of the measured linewidth (Fig. 6c inset). In contrast, when using a red-detuned pump, increasing the optical power dampens the mechanical motion and broadens the linewidth, in agreement with expectations for a dispersively coupled device [35]. We verified that excitation of the LGP resonances is required both to transduce the motion and observe self-oscillation through a series of control experiments (Supplement 1, Section 6). These experiments show that motion signals measured both in ambient conditions (Fig. 3a) and in vacuum (Fig. 6a) abruptly disappear when displacing the laser spot by ≈ 1 μm in either direction along the cantilever from its focused position on the LGPR. Furthermore, they show that the input polarization must be oriented along the cuboid long axis (exciting the LGP resonance) to observe transduction and self-oscillation. Thus, for conditions under which the LGP mode is not excited, we observe no optomechanical effects for input optical powers up to a maximum of ≈ 3 mW in our setup.

For pump power just above threshold, the free-running PMO frequency f_0 and its amplitude are stable and characterized by a narrow linewidth (dark red curve, Fig. 6b). Similarly, for pump power above ≈ 1500 μW the PMO frequency is stable and displays a narrow linewidth on top of a broad background (gold curve, Fig. 6b) with saturated amplitude. However, pumping near the high end of the transition region, but below saturation, produces apparently chaotic behavior characterized by rapid variations in frequency and amplitude, consistent with previous observations [36]. The red curve in Fig. 6b represents one such example of chaotic behavior, averaged with 100 Hz bandwidth (Supplement 1, Section 7).

The PMO is driven by time-delayed thermal feedback between the gap-size dependent absorption in the LGPR and thermal bimorph actuation of the cantilever. For a given temperature increase ΔT, the bimorph closes the gap with gain $g_\mathrm{B} \equiv \partial x/\partial \Delta T \approx 45$ pm K^{-1} at the location of the LGPR (Supplement 1, Section 3). The finite time constant $\tau_\mathrm{t} \approx 1.5$ μs of the thermal response causes a phase-delay between motion and bimorph actuation, resulting in a complex-valued effective photothermal spring that applies a force component proportional to velocity [30,31,37]. For blue-detuned pumping of the dispersive LGPR, the absorbance gain $g_\mathrm{A} \equiv \partial A/\partial x$ is negative and the photothermal spring contributes negative damping to the system, adding energy to the mechanical oscillation each cycle. Self-oscillation occurs when the overall photothermal gain exceeds intrinsic mechanical losses, occurring for a threshold pump power

$$P_0 \geq \frac{m_\mathrm{th}\, c_\mathrm{p}}{|g_\mathrm{A}|} \frac{\omega_\mathrm{m}^2 + \tau_\mathrm{t}^{-2}}{Q_\mathrm{m}\, \omega_\mathrm{m}\, g_\mathrm{B}}, \quad (1)$$

where $m_\mathrm{th} \approx 4.6$ pg is the cantilever thermal mass, $Q_\mathrm{m} = 1655 \pm 35$ is the native, cold-cavity mechanical quality factor, and $\omega_\mathrm{m} = 2\pi \cdot 4030$ kHz is the resonant mechanical frequency; a mass-specific heat of c_p = 1100 J kg^{-1} K^{-1} is assumed (Supplement 1, Section 8) [33].

Figure 7 shows the numerically calculated optical absorbance gain landscape for our system, with the blue and red-detuned experimental conditions used for Fig. 6b indicated as white and black data points, respectively. For the blue detuned case, we expect $g_\mathrm{A} = (-1.6 \pm 0.2)$ pm^{-1}, based on the value of the

gap from the atomic force micrograph (Fig. 1b) of a test device on the same chip and its propagated uncertainty. AFM deflection measurements of several additional test devices show that the change in curvature from device-to-device on the same chip is minimal (Supplement 1, Section 2). We therefore expect the AFM measurement in Fig. 1b to be a reliable predictor of the curvature of the experimentally measured devices, as this test device appeared on the same chip. Using the expected values of g_{A}, g_{B}, parameters from our system, and Eq. (1), we find a predicted lasing threshold power of (1080 $\pm$ 23) μW, in good agreement with observations.

The observed threshold power of our PMO is large compared to other optomechanical oscillators, which can have thresholds from tens to hundreds of microwatts [32,38–40]. However, the large threshold in our case does not represent an inherent inefficiency of the single-LGPR transduction, and could be further improved by optimizing mechanical and thermal characteristics of the device and the experimental conditions. For instance, we have chosen a dispersive LGPR very close to the cantilever base to demonstrate both self-oscillation and cooling. Moving it away from the base quadratically increases the bimorph gain g_{B}, while only slowly decreasing g_{A}. Reducing the cantilever thickness also increases g_{B} by lowering the bending stiffness while also reducing the frequency and the thermal mass. Finally, an additional 3× reduction in threshold (increase of g_{A}) can be realized by improving the pump numerical aperture (NA) from 0.3, our current experimental limitation, to 0.9. In sum, these improvements can bring the threshold to ≈ 50 μW or lower. Nevertheless, the ability to tune the PMO dynamics by adjusting the LGPR position and the ability to engineer sub-diffraction systems clearly distinguishes our system from the previously studied optically driven oscillators.

Injection locking the PMO

The PMO is built upon the ability of the LGPR to localize and enhance optical, thermal, and mechanical interactions. The electrical degree of freedom available can not only tune these interactions as we show above, but can also directly influence the dynamic behavior of the PMO. Specifically, the integrated electrostatic actuator can deliver a weak mechanical force to the oscillating PMO, whose large-amplitude output synchronizes in phase to the applied radio-frequency (RF) tone – injection locking the PMO [41–46].

To perform injection locking, we apply an input stimulus of slowly time-varying frequency f_{in} to the device operating at a free-running frequency f_0 ≈ 3980 kHz and pumped with 2 mW of optical power. Figure 8a shows a log-scale contour plot of the power spectral density of the transduced motion as f_{in} is swept across f_0; linescans at various points are given in Fig. 8b. Within a band defined by $f_0 \pm f_{\mathrm{L}}/2$, the PMO frequency follows f_{in} synchronously, whereas outside this band, frequency pulling of f_0 toward f_{in} is evident from the significant curvature in f_0, as are multiple distortion sidebands. These spectral signatures (locking, pulling, and sidebands) are theoretically described via

$$f_p = f_{\mathrm{in}} + (p+1)\delta f \sqrt{1 - \left(\frac{f_{\mathrm{L}}/2}{\delta f}\right)^2}, \tag{2}$$

where $\delta f \equiv f_{\mathrm{in}} - f_0$ is the detuning of the injection signal, p is the sideband order, and f_{L} is the injection locking range [46,47]. Interestingly, sonification of the PMO data clearly reveals the spectral signatures predicted by Eq. (2), including a clearly audible onset of locking (Supplement 1, Section 9 and Supplement 3). As such, this data representation technique may prove useful for future analyses of time-varying data from regenerative oscillators [48].

The locking range is governed by the ratio of the injected amplitude to the amplitude of the free running PMO. In our experiments, the simple linear form of the range is given by

$$f_{\mathrm{L}} = \frac{\omega_{\mathrm{m}}}{2\pi}\frac{1}{Q_{\mathrm{m}}}\frac{x_{\mathrm{inj}}}{x_{\mathrm{free}}} = \frac{\omega_{\mathrm{m}}}{2\pi}\frac{x_{\mathrm{in}}}{x_{\mathrm{free}}}, \quad (3)$$

where x_{free} is the LGPR displacement in the free-running PMO. The commonly used [41] injected displacement near resonance x_{inj} is re-expressed through the amplitude $x_{\mathrm{in}} = x_{\mathrm{inj}}/Q_{\mathrm{m}}$, which is the experimentally observable displacement response to the stimulus applied far below the resonance frequency. Dashed blue lines in Fig. 8a correspond to Eq. (2), wherein f_0 and f_{L} are used as fitting parameters with values of 3980 kHz and 27 kHz, respectively.

While the major features of the injection locking behavior are captured using Eq. (2), there are significant deviations from this linear theory. The total observed range (36.9 kHz) at this injection amplitude extends beyond the range expected from the fit of Eq. (2) (Fig. 8c); this trend is observed for all x_{in} applied. The extended locking range is accompanied by the appearance of pronounced sidebands (green curve, Fig. 8b) indicative of oscillations that likely result from either nonlinear interaction between the drive amplitude and the free-running PMO, or from nonlinearities in the optomechanical transduction [49]. The amplitude and number of these sidebands increases significantly with increased injection amplitude (Supplement 1, Section 10). Furthermore, at large injection amplitudes the total observed locking range is smaller than that predicted by Eq. (3), as determined from calibrated displacement data for $x_{\mathrm{in}}/x_{\mathrm{free}}$. However, the measured range approaches the linear prediction Eq. (3) in the low x_{in} limit (Fig. 8d), indicating that linear injection locking theory is a valid quantitative description for our system at weak injection amplitude. This is expected, because the simple linear theory is valid only for low injection powers $x_{\mathrm{inj}}/x_{\mathrm{free}} < 1$ or $x_{\mathrm{in}}/x_{\mathrm{free}} < Q_{\mathrm{m}}^{-1}$.

The injection locking results (Fig. 8b) show that input displacements as small as 10 pm can be amplified by a large factor of $x_{\mathrm{free}}/x_{\mathrm{in}} \approx 100$ over a bandwidth (the locking range) of 20 kHz to 50 kHz, an order of magnitude larger than the cold-cavity mechanical linewidth of approximately 2 kHz. Conversely, in the absence of optical pumping, only the stimuli within the native linewidth will produce a strong response, amplified by Q_{m}. PMO locking significantly extends the frequency range over which the input signals are amplified, and therefore the technique is potentially useful for amplifying and reading out frequency of weak FM tone signals. For instance, the locked PMO could tracking frequency variations of another, coupled nanomechanical oscillator whose amplitude is otherwise too weak or inaccessible for direct detection. Notably, the PMO locking may be instrumental for reading out a different mechanical mode of the same or a coupled nanomechanical system, including nonlinear coupled modes at integer multiples of the oscillator fundamental frequency [50]. The PMO can thus perform the function of a mechanical amplifier and phase-locked loop for frequency detection of various weak processes occurring at the nanoscale [51].

Conclusion

We have demonstrated a new active plasmomechanical system with integrated electrical tuning and excitation that successfully localizes opto-thermo-mechanical interactions to sub-diffraction volumes, leading to facile electro-optic modulation, selective nanomechanical motion transduction, and the first-ever demonstration of an injection-locked plasmomechanical oscillator. The point-like LGPRs mediate both optomechanical and thermo-mechanical coupling *via* their spatial location. Varying the plasmonic gap tunes devices through dispersive and reactive coupling regimes with distinct spectral responses, and controls the threshold power of the plasmomechanical oscillator. Through injection locking, we have shown that the plasmomechanical oscillator can synchronize to and amplify weak mechanical stimuli for nanomechanical sensing. Electrical tuning and switching of individually addressable plasmomechanical systems are promising building blocks for realizing extended, high-spatial-resolution light modulator arrays and tunable metasurfaces with applications in light-beaming, and optical pulse and wavefront shaping.

Acknowledgment. We thank R. Ilic and I. Brener for meticulous readings of the manuscript and fruitful discussions.

See Supplements 1–3 for supporting content.

References

1. M. I. Stockman, "Nanoplasmonics: past, present, and glimpse into future," Opt. Express **19**, 22029–22106 (2011).
2. D. J. Bergman and M. I. Stockman, "Surface Plasmon Amplification by Stimulated Emission of Radiation: Quantum Generation of Coherent Surface Plasmons in Nanosystems," Phys. Rev. Lett. **90**, 027402 (2003).
3. J. N. Anker, W. P. Hall, O. Lyandres, N. C. Shah, J. Zhao, and R. P. Van Duyne, "Biosensing with plasmonic nanosensors," Nat. Mater. **7**, 442–453 (2008).
4. B. J. Roxworthy, K. D. Ko, A. Kumar, K. H. Fung, E. K. C. Chow, G. L. Liu, N. X. Fang, and K. C. Toussaint, "Application of Plasmonic Bowtie Nanoantenna Arrays for Optical Trapping, Stacking, and Sorting," Nano Lett. **12**, 796–801 (2012).
5. Y. Zhao, A. A. E. Saleh, and J. A. Dionne, "Enantioselective Optical Trapping of Chiral Nanoparticles with Plasmonic Tweezers," ACS Photonics **3**, 304–309 (2016).
6. S. V. Boriskina, H. Ghasemi, and G. Chen, "Plasmonic materials for energy: From physics to applications," Mater. Today **16**, 375–386 (2013).
7. M. Kauranen and A. V Zayats, "Nonlinear plasmonics," Nat. Photonics **6**, 737–748 (2012).
8. M. S. Tame, K. R. McEnery, Ş. K. Özdemir, J. Lee, S. A. Maier, and M. S. Kim, "Quantum plasmonics," Nat. Phys. **9**, 329–340 (2013).
9. R. Thijssen, E. Verhagen, T. J. Kippenberg, and A. Polman, "Plasmon nanomechanical coupling for nanoscale transduction," Nano Lett. **13**, 3293–3297 (2013).
10. B. J. Roxworthy and V. A. Aksyuk, "Nanomechanical motion transduction with a scalable localized gap plasmon architecture," Nat. Commun. **7**, 13746 (2016).
11. J. Y. Ou, E. Plum, J. Zhang, and N. I. Zheludev, "Giant nonlinearity of an optically reconfigurable plasmonic metamaterial," Adv. Mater. **28**, 729–733 (2016).
12. H. Zhu, F. Yi, and E. Cubukcu, "Plasmonic metamaterial absorber for broadband manipulation of mechanical resonances," Nat. Photonics **10**, 709–714 (2016).
13. B. Dong, X. Chen, F. Zhou, C. Wang, H. F. Zhang, and C. Sun, "Gigahertz All-Optical Modulation Using Reconfigurable Nanophotonic Metamolecules," Nano Lett. **16**, 7690–7695 (2016).
14. E. Prodan, C. Radloff, N. J. Halas, and P. Nordlander, "A hybridization model for the plasmon response of complex nanostructures.," Science **302**, 419–22 (2003).
15. V. A. Fedotov, N. Papasimakis, E. Plum, A. Bitzer, M. Walther, P. Kuo, D. P. Tsai, and N. I. Zheludev, "Spectral collapse in ensembles of metamolecules," Phys. Rev. Lett. **104**, 223901 (2010).
16. J. B. Khurgin, "How to deal with the loss in plasmonics and metamaterials," Nat. Nanotechnol. **10**, 2–6 (2015).
17. N. I. Zheludev and E. Plum, "Reconfigurable nanomechanical photonic metamaterials," Nat.

Nanotechnol. **11**, 16–22 (2016).

18. M. Hossein-Zadeh, H. Rokhsari, A. Hajimiri, and K. Vahala, "Characterization of a radiation-pressure-driven micromechanical oscillator," Phys. Rev. A **74**, 023813 (2006).
19. K. Y. Fong, M. Poot, X. Han, and H. X. Tang, "Phase noise of self-sustained optomechanical oscillators," Phys. Rev. A **90**, 023825 (2014).
20. K. L. Ekinci and M. L. Roukes, "Nanoelectromechanical systems," Rev. Sci. Instrum. **76**, 061101 (2005).
21. L. Koster, H. Gerth, and H. Haase, "Thermal modes and their application to turbogenerator rotors," Electr. Eng. **82**, 135–144 (2000).
22. M. Maldovan, "Sound and heat revolutions in phononics.," Nature **503**, 209–217 (2013).
23. T. Søndergaard and S. Bozhevolnyi, "Slow-plasmon resonant nanostructures: Scattering and field enhancements," Phys. Rev. B **75**, 073402 (2007).
24. M. Li, W. H. P. Pernice, and H. X. Tang, "Reactive cavity optical force on microdisk-Coupled nanomechanical beam waveguides," Phys. Rev. Lett. **103**, 223901 (2009).
25. B. S. Dennis, M. I. Haftel, D. A. Czaplewski, D. Lopez, G. Blumberg, and V. A. Aksyuk, "Compact nanomechanical plasmonic phase modulators," Nat. Photonics **9**, 267–273 (2015).
26. T.-Z. Shen, S.-H. Hong, and J.-K. Song, "Electro-optical switching of graphene oxide liquid crystals with an extremely large Kerr coefficient," Nat. Mater. **13**, 394–399 (2014).
27. M. Wu, A. C. Hryciw, C. Healey, D. P. Lake, H. Jayakumar, M. R. Freeman, J. P. Davis, and P. E. Barclay, "Dissipative and dispersive optomechanics in a nanocavity torque sensor," Phys. Rev. X **4**, 021054 (2014).
28. C. Metzger and K. Karrai, "Cavity cooling of a microlever," Nature **432**, 1002–1005 (2004).
29. J. B. Khurgin, M. W. Pruessner, T. H. Stievater, and W. S. Rabinovich, "Laser-rate-equation description of optomechanical oscillators," Phys. Rev. Lett. **108**, 223904 (2012).
30. M. Zalalutdinov, A. Zehnder, A. Olkhovets, S. Turner, L. Sekaric, B. Ilic, D. Czaplewski, J. M. Parpia, and H. G. Craighead, "Autoparametric optical drive for micromechanical oscillators," Appl. Phys. Lett. **79**, 695–697 (2001).
31. C. Metzger, M. Ludwig, C. Neuenhahn, A. Ortlieb, I. Favero, K. Karrai, and F. Marquardt, "Self-Induced oscillations in an optomechanical system driven by bolometric backaction," Phys. Rev. Lett. **101**, 133903 (2008).
32. R. De Alba, T. S. Abhilash, R. H. Rand, H. G. Craighead, and J. M. Parpia, "Low-Power Photothermal Self-Oscillation of Bimetallic Nanowires," Nano Lett. **17**, 3995–4002 (2017).
33. S. Zaitsev, A. K. Pandey, O. Shtempluck, and E. Buks, "Forced and self-excited oscillations of an optomechanical cavity," Phys. Rev. E **84**, 046605 (2011).
34. B. D. Hauer, C. Doolin, K. S. D. Beach, and J. P. Davis, "A general procedure for thermomechanical calibration of nano/micro-mechanical resonators," Ann. Phys. **339**, 181–207 (2013).
35. M. Aspelmeyer, T. J. Kippenberg, and F. Marquardt, "Cavity optomechanics," Rev. Mod. Phys. **86**, 1391–1452 (2014).
36. M. Bagheri, M. Poot, L. Fan, F. Marquardt, and H. X. Tang, "Photonic cavity synchronization of

nanomechanical oscillators," Phys. Rev. Lett. **111**, 213902 (2013).

37. J. B. Khurgin, M. W. Pruessner, T. H. Stievater, and W. S. Rabinovich, "Optically pumped coherent mechanical oscillators: the laser rate equation theory and experimental verification," New J. Phys. **14**, 105022 (2012).

38. X. Luan, Y. Huang, Y. Li, J. F. McMillan, J. Zheng, S.-W. Huang, P.-C. Hsieh, T. Gu, D. Wang, A. Hati, D. A. Howe, G. Wen, M. Yu, G. Lo, D.-L. Kwong, and C. W. Wong, "An integrated low phase noise radiation-pressure-driven optomechanical oscillator chipset.," Sci. Rep. **4**, 6842 (2014).

39. M. Hossein-Zadeh and K. J. Vahala, "An optomechanical oscillator on a silicon chip," IEEE J. Sel. Top. Quantum Electron. **16**, 276–287 (2010).

40. T. J. Kippenberg, H. Rokhsari, T. Carmon, A. Scherer, and K. J. Vahala, "Analysis of Radiation-Pressure Induced Mechanical Oscillation of an Optical Microcavity," Phys. Rev. Lett. **95**, 033901 (2005).

41. R. Adler, "A study of locking phenomena in oscillators," Proc. IRE **34**, 351–357 (1946).

42. M. Zhang, G. S. Wiederhecker, S. Manipatruni, A. Barnard, P. McEuen, and M. Lipson, "Synchronization of micromechanical oscillators using light," Phys. Rev. Lett. **109**, 233906 (2012).

43. S. Knünz, M. Herrmann, V. Batteiger, G. Saathoff, T. W. Hänsch, K. Vahala, and T. Udem, "Injection locking of a trapped-ion phonon laser," Phys. Rev. Lett. **105**, 013004 (2010).

44. M. Wang, C. Zhao, X. Miao, Y. Zhao, J. Rufo, Y. J. Liu, T. J. Huang, and Y. Zheng, "Plasmofluidics: Merging Light and Fluids at the Micro-/Nanoscale," Small **11**, 4423–4444 (2015).

45. Y. Y. Liu, J. Stehlik, M. J. Gullans, J. M. Taylor, and J. R. Petta, "Injection locking of a semiconductor double-quantum-dot micromaser," Phys. Rev. A **92**, 053802 (2015).

46. A. E. Siegman, *Lasers* (University Science Books, 1986).

47. Y. Liu, E. N. Mills, and R. J. Composto, "Tuning optical properties of gold nanorods in polymer films through thermal reshaping," J. Mater. Chem. **19**, 2704 (2009).

48. W. L. Diaz-Merced, R. M. Candey, N. Brickhouse, M. Schneps, J. C. Mannone, S. Brewster, and K. Kolenberg, "Sonification of astronomical data," Proc. Int. Astron. Union **7**, 133–136 (2011).

49. H. Rokhsari, T. J. Kippenberg, T. Carmon, and K. J. Vahala, "Radiation-pressure-driven micro-mechanical oscillator," Opt. Express **13**, 5293–5301 (2005).

50. D. Antonio, D. H. Zanette, and D. López, "Frequency stabilization in nonlinear micromechanical oscillators," Nat. Commun. **3**, 806 (2012).

51. L. G. Villanueva, R. B. Karabalin, M. H. Matheny, E. Kenig, M. C. Cross, and M. L. Roukes, "A Nanoscale Parametric Feedback Oscillator," Nano Lett. **11**, 5054–5059 (2011).

52. R. Thijssen, T. J. Kippenberg, A. Polman, and E. Verhagen, "Plasmomechanical resonators based on dimer nanoantennas," Nano Lett. **15**, 3971–3976 (2015).

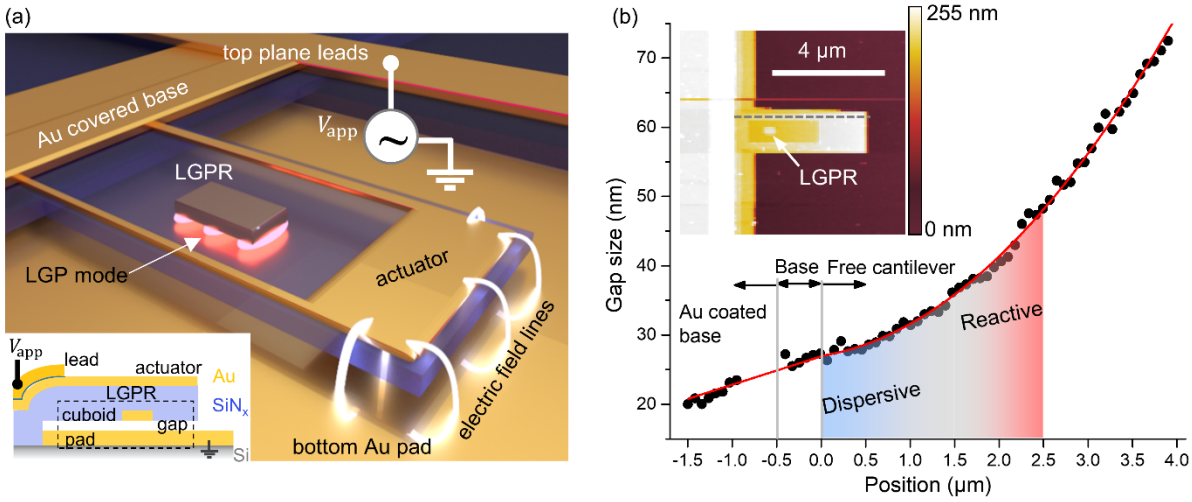

Fig. 1. (a) Illustration of the device architecture. The inset shows a side view of the device structural layers and elements. Red color represents the 3rd order localized gap plasmon mode. While lines represent actuator electric field. (b) Line scan of an atomic force micrograph (gray dashed line, inset) of a 4 µm cantilever with an integrated LGPR on the same chip as the devices studied in this work. The total gap size is the sum of the nominal 20 nm sacrificial layer thickness and the upward deflection due to residual stress; the profile is corrected for the ≈ 130 nm lead thickness. Red lines are fits that indicate the upward deflection of the structure due to tilt at the gold coated base (linear) and the curved shape of the free cantilever (parabolic). Regions of expected dispersive and reactive optomechanical coupling, based on simulation data, are indicated by the shaded region.

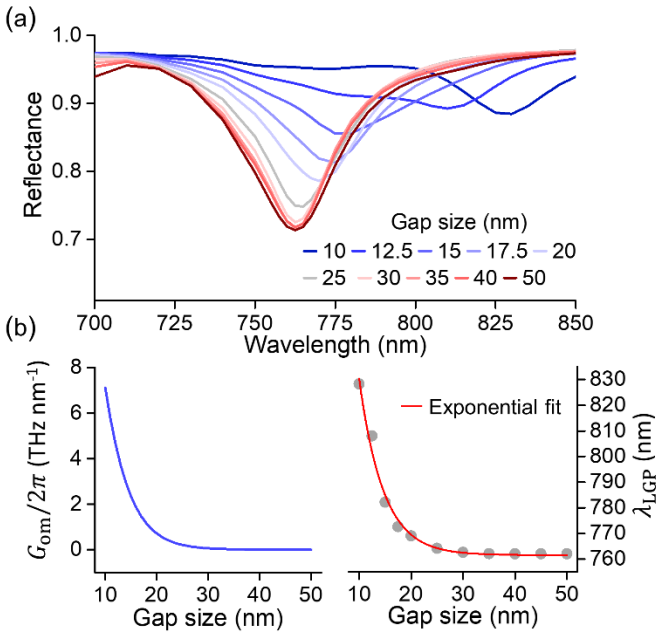

Fig. 2. Finite element calculations of (a) the reflectance of the LGP resonance as a function of gap, the arrows illustrate the direction of change of the reflectance dip with decreasing gap in the different coupling regimes. (b) Extracted LGP wavelength (right panel) with exponential fit and calculated dispersive optomechanical coupling constant (left panel).

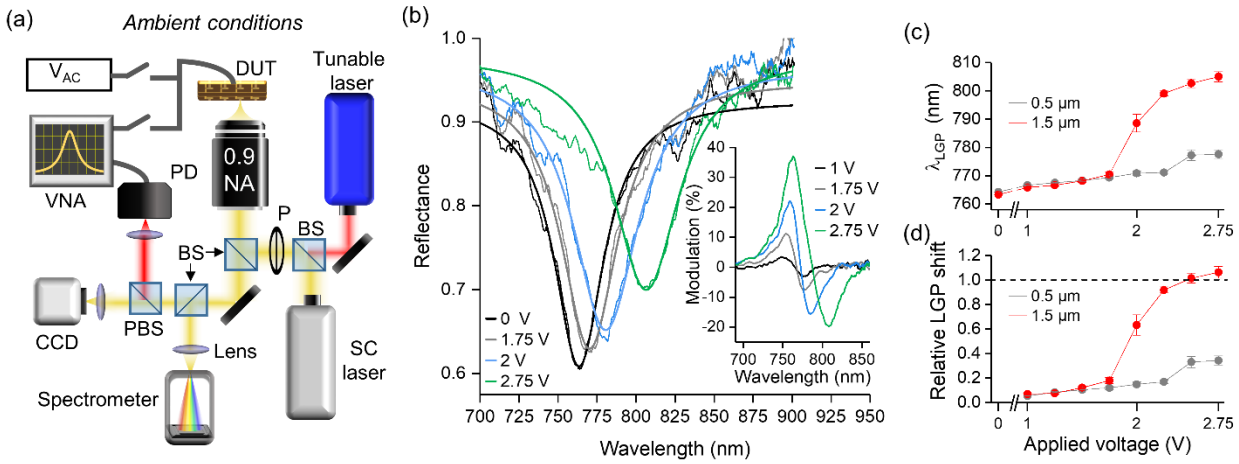

Fig. 3. Optical modulation with LGPRs. (a) Experimental setup for modulation and transduction in ambient conditions. Components are: (P)BS – (polarizing) beam splitter, P – polarizer, PD – photodiode, VNA – vector network analyzer, DUT – device under test. (b) Experimentally measured spectral reflectance of a single LGPR as a function of applied voltage with Lorentzian fits; the inset shows the measured amplitude modulation of the electrically actuated LGPR. Reflectance spectra are normalized relative to the laser reference spectrum measured by focusing the broadband probe laser on the gold pad through the cantilever but displaced from the LGPR ≈ 1 μm. Reference measurements are taken within 1 second of each spectrum measurement to minimize effects of laser spectrum drift. (c) Experimentally measured LGP wavelengths and (d) relative shift of the LGP resonance as a function of voltage; uncertainties are derived from Lorentzian fits.

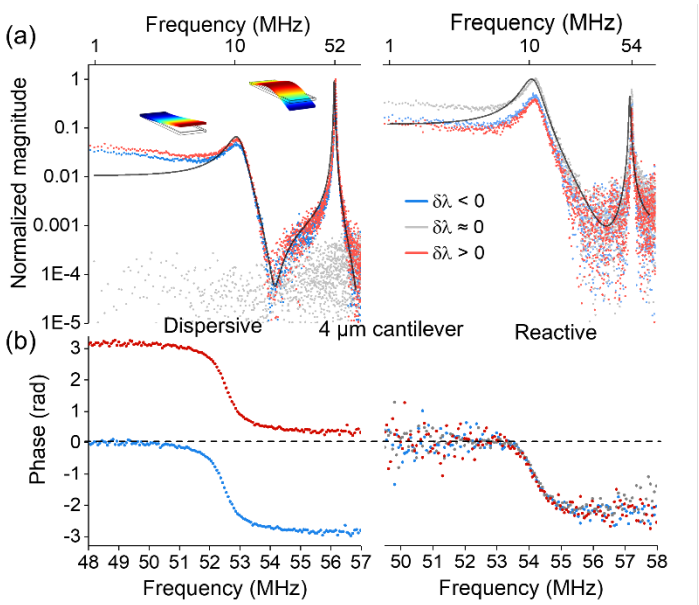

Fig. 4. (a) Normalized magnitude of electrostatically driven motion transduced, in ambient air conditions, by a dispersive (left panels) and reactive (right panels) LGPR, measured with different probe laser detuning. Black lines correspond to a best fit of two Lorentzian functions added coherently; inset cartoons depict the shape of the flexural mechanical modes. The change in relative strength of the resonances between the left and right panels indicate selective mode transduction. The dispersive case illustrates that the LGPR motion is described by a coherent superposition of the displacement from two flexural modes: the modal displacements are cancelling each other out at the LGPR position near the 20 MHz excitation frequency. (b) Motion phase near the second order flexural mode resonance. Dispersive coupling produces opposite phase at different signs of detuning, indicating a change in the sign of the reflectance derivative $sign[\partial_x R]$ with detuning. Reactively coupled devices produce the same phase ($sign[\partial_x R]$) regardless of detuning.

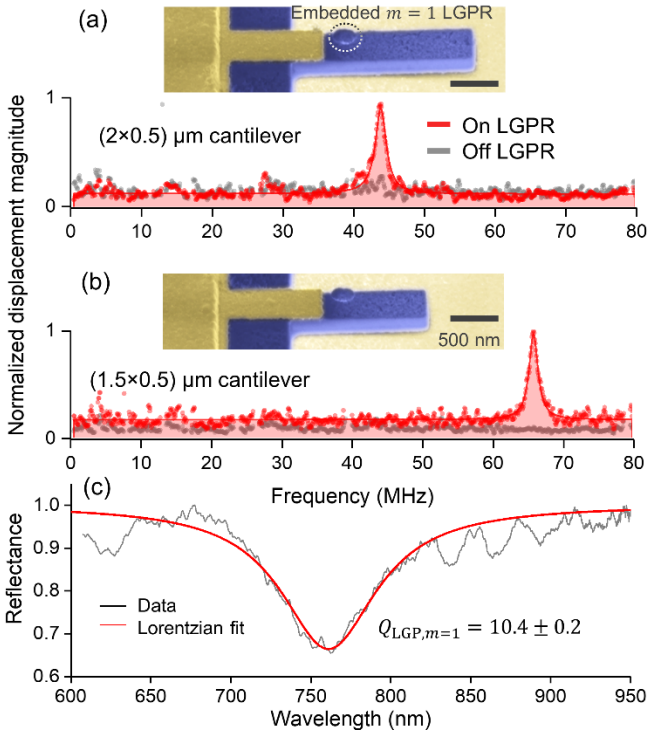

Fig. 5. Scanning electron micrographs and measured motion signals for electrostatically actuated 500 nm wide cantilevers with (a) 2 μm length and (b) 1.5 μm length. The ≈ (90×75×40) nm^3 LGPR, embedded on the underside of the cantilever, forms a visible 'bulb' through the thickness which protrudes from the top of the silicon nitride. (c) Reflection spectrum from the LGPR showing the $m = 1$ LGP mode.

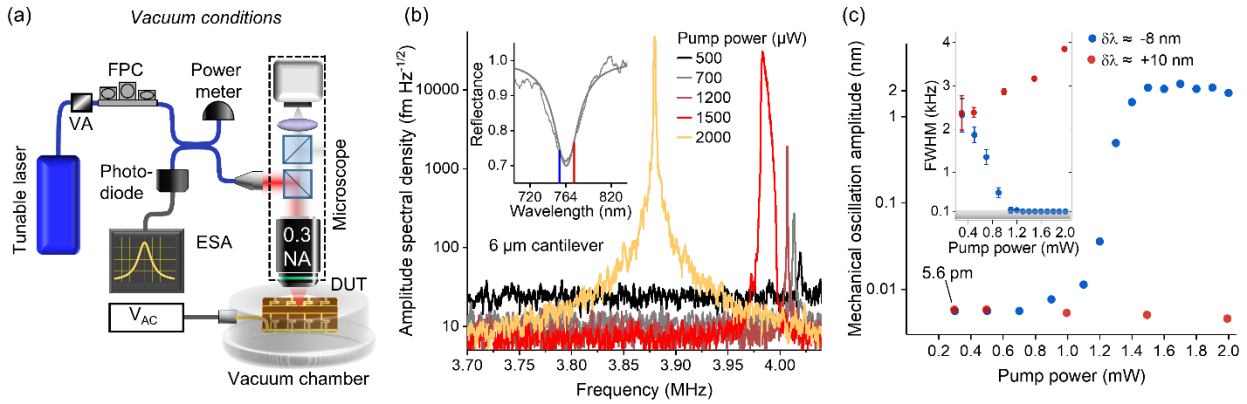

Fig. 6. (a) Experimental setup for vacuum conditions. Components are: VA – variable attenuator, FPC – fiber polarization controller, ESA – Electronic spectrum analyzer. (b) Mechanical amplitude spectral density for optical pump powers in different regimes of below threshold (black, gray), above threshold (dark red), and saturated (gold). There exists an apparently chaotic regime [36] for pumping near saturation (red curve, 1500 μW), whereby the amplitude and frequency fluctuate rapidly. In this case, the apparent broadened linewidth is a result of rapid frequency variation during the instrument averaging. The reduction in noise floor with increasing pump power is a result of decreased imprecision noise. The inset shows the reflectance spectrum of the LGPR with negative and positive experimental wavelength detunings marked with blue and red lines, respectively. (c) Mechanical oscillation amplitude of the LGPR on a logarithmic scale as function of pump power for negative (blue dots) and positive (red dots) wavelength detuning; inset shows corresponding mechanical linewidths and their uncertainties determined from Lorentzian fits. The shaded gray region indicates the measurement resolution limit.

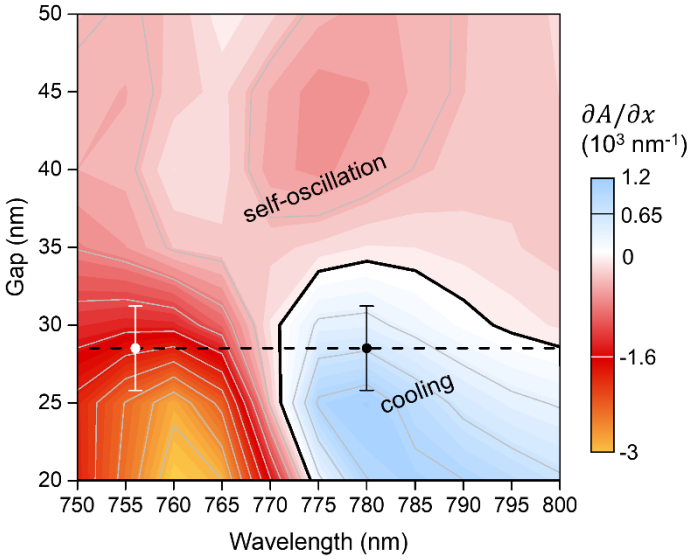

Fig. 7. Calculated plasmomechanical absorbance gain landscape (red-yellow: excitation, blue: cooling) with experimental measurement points for negative (white dot) and positive (black dot) detuning; gap value and uncertainty is from the AFM measurements. The solid black line indicates the zero-gain contour and dotted line indicates the expected gap of the device.

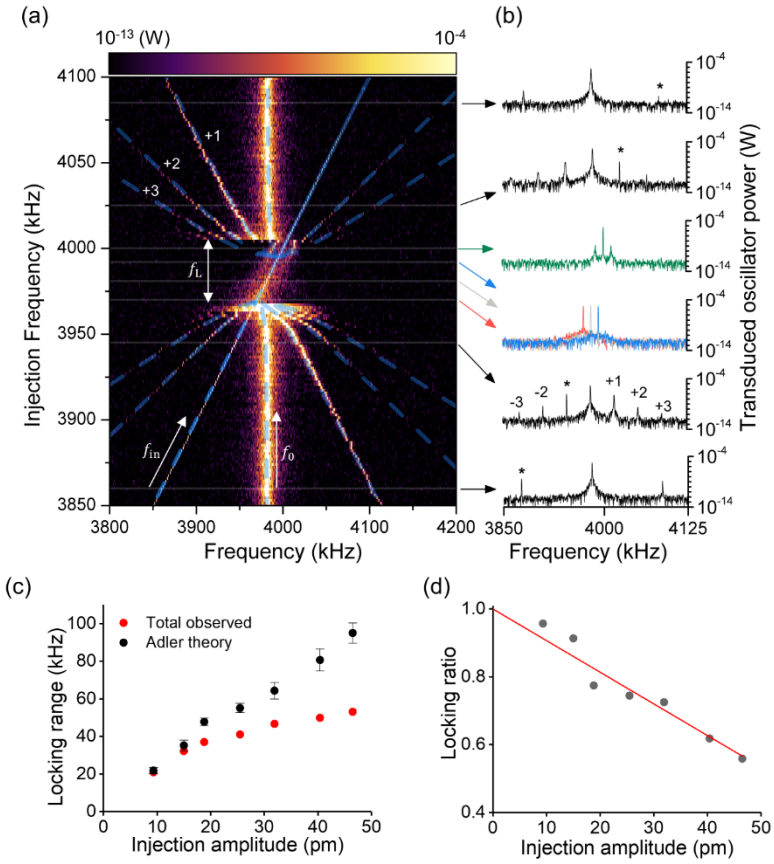

Fig. 8. (a) Log-scale contour plot of the motion power spectral density of the plasmomechanical oscillator (free-running frequency f_0) for varying injection frequency f_{in} at an injection amplitude of $x_{\mathrm{in}} \approx 25$ pm . The oscillator is locked to the input RF tone and follows f_{in} over the interval f_{L}. (b) Line cuts of the motion power spectra for unlocked (black curves, f_{in} marked by * symbol) and locked (red, gray, blue, and green curves) operation, plotted on log-scale. Numerical annotations represent the distortion sideband order up to a value of ± 3. Additional sidebands appearing at the top of the locking range (green curve) are distinct from the distortion sidebands outside the locking range predicted by Eq. (2), and are likely the result of intermodulation between the applied actuated displacement and the oscillator. (c) Total observed locking range (red) (i.e., central rectangular band in (a)) and the Adler theory prediction $f_{\mathrm{L}} = \omega_{\mathrm{m}}/2\pi \; x_{\mathrm{in}}/x_{\mathrm{free}}$ (black); these quantities agree at low injection amplitude. The predicted values correspond to the average ratio of the injection displacement to the free-running displacement $x_{\mathrm{in}}/x_{\mathrm{free}}$ measured at far-detuned f_{in}, ranging from 3800 kHz to 3825 kHz; uncertainties are one standard deviation from multiple detunings. (d) Ratio of the total observed range to the theoretical predictions from Adler's theory, which shows a linear relationship converging to unity for weak injected signals, for which the Adler theory is valid.

Supplementary Information

1. Fabrication Procedure

Devices are fabricated monolithically from a bare Si chip using repeated steps of aligned electron-beam lithography (aEBL), as depicted in Fig. S1. Unless otherwise specified, each EBL exposure used a bilayer resist of 495k/950k molecular weight polymethyl methacrylate with total thickness three times greater than the total thickness of deposited metal layer. In the process, metal layers are formed using electron-beam evaporation and liftoff (LO) in a 1:1 by volume solution of acetone and methylene chloride. The first layer comprises a 5 nm Ti adhesion layer, 50 nm Au pad, and 20 nm Cr sacrificial layer. Cuboids with nominal dimensions of approximately (350×160×40) nm^3 are then formed with an aligned EBL (aEBL) exposure. The nitride device layer is deposited at 180 °C using a plasma-enhanced chemical vapor deposition (PECVD) process incorporating inductively-coupled plasma (ICP) during the deposition. Stress in the nitride film is controlled via ICP power to fall within the range from 175 MPa to 225 MPa. Actuators, formed using a third aEBL+LO step, are composed of 15 nm Au atop a 3 nm Ti adhesion layer. Next, electrical leads and bond pads are formed from a 10 nm Ti, 120 nm Au stack using a fourth aEBL+LO step. A final aEBL step using a commercial high-resolution resist forms a dry-etch mask, which is transferred to the nitride using reactive-ion etching. The exposed Cr sacrificial layer is etched using a solution of ceric ammonium nitrate and chips are finalized by critical point drying in liquid CO_2. Devices are finalized by wire-bonding chips to a printed circuit board connectorized with coaxial RF jacks.

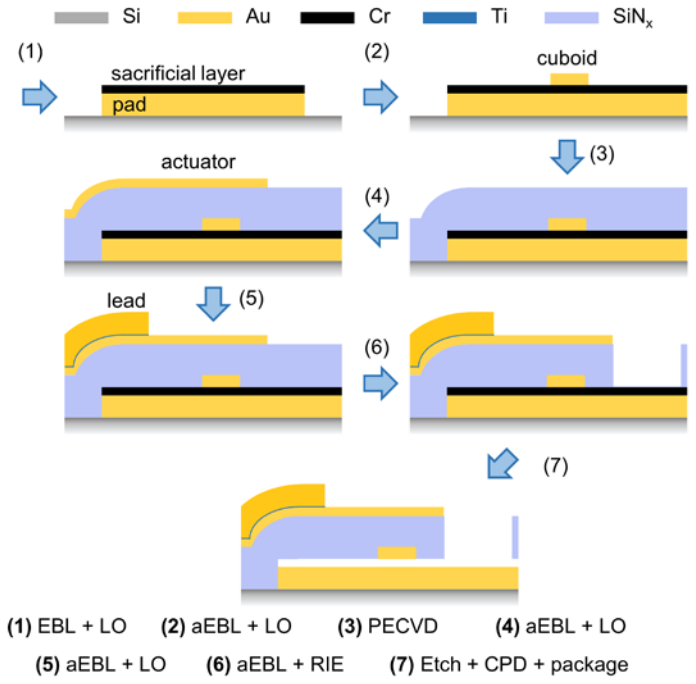

Fig S1. Process flow for the fabricating devices. Processes are: (a)EBL – (aligned) electron beam lithography, LO – liftoff, PECVD – plasma-enhanced chemical vapor deposition, RIE – reactive-ion etching, Etch – wet-chemical etching of Cr, CPD – critical point drying. The cutaway near the cuboid is included for illustration purposes and is not present in actual devices.

2. Atomic Force Microscopy Measurements

Residual stress and stress gradients occur in the devices as a result of the nitride deposition process. The stress gradient causes released cantilevers to curl away from the underlying substrate, affecting the final gap of the plasmonic resonator. This curvature is approximately uniform for each device on any given chip, such that the atomic force micrograph of the test device in the main text gives a reliable predictor of the curvature of experimentally measured devices, from the same chip. To quantify the variation within a chip, we perform additional AFM measurements on a set of test devices fabricated on a separate chip. Figure S2 shows the measurements performed on three devices selected randomly on this chip. Each chip is fabricated separately and due to variations in the fabrication process these devices have a larger intrinsic stress and stress gradient, and thus a larger deflection d than the devices in the main text. However, it is evident that there is only a small variation between devices in the overall deflection and in the curvature from device-to-device; we find from parabolic fits of the form $d = bx + c\,x^2$ to the linescans of the deflected shape images that the curvature varies by ≈ 10 %, which indicates good uniformity of the fabrication process. This variation is calculated via σ_c/c, where σ_c is the standard deviation of the c parameter calculated from the fit. The standard deviation of the deflection at x = 0.5 µm is measured to be 2.7 nm.

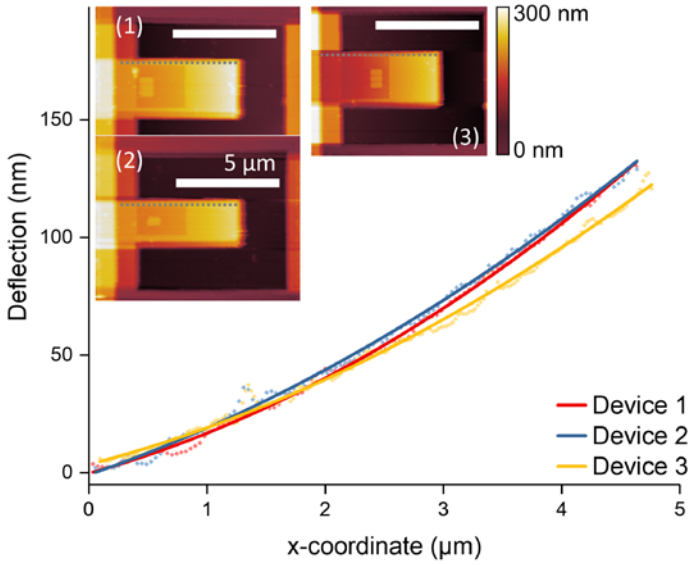

Fig. S2. Atomic force microscopy measurements. Deflection line profiles of three test devices on the same chip (separate from the main text devices), which was fabricated in parallel with those studied in the main text. Solid lines are parabolic fits to the deflected shapes, which are extracted from the two-dimensional images (inset) at locations indicated by the gray-dotted lines.

3. Finite-Element Modelling

We use a commercial finite-element solver to model electromagnetic, mechanical, and thermal properties of the devices. Two model geometries are used. The first (Fig. S3a) is used for electromagnetic modelling and consists of a cylindrical domain comprising a 165 nm thick, 2 µm wide silicon nitride beam cantilever placed over an Au pad (atop a Si substrate) separated by a variable air gap. A 15 nm thick Au actuator is placed atop the beam with an approximately (2.5×1.75) µm^2 opening filled with air and centered above a cuboid with dimensions (350×160×40) nm^3; a fillet with 15 nm radius of curvature is applied to all edges of the cuboid to avoid spurious electrical field effects. A Gaussian beam with focal point at the surface of the Au pad and spot radius of 0.6 λ_0/NA for numerical

aperture NA = 0.3 or 0.9 and varying input wavelength λ_0 is introduced *via* a port boundary condition above the structure. The remaining boundary conditions include a second port at the bottom of the Si substrate, perfect magnetic conductors for symmetry, and perfectly matched layers along the top, bottom, and outer edges to prevent reflections into the computational domain. Reflectance is calculated using S-parameters $R = |S_{11}|^2$, where S_{11} corresponds to the top port. Absorption is calculated using a loss-integral formulation, via

$$A \equiv \frac{1}{P_0}\int \frac{1}{2}\mathrm{Re}[\boldsymbol{J}\cdot\boldsymbol{E}^*]\mathrm{d}V, \tag{S1}$$

where P_0 is the power launched into the domain. The integral of the inner product of current density $\boldsymbol{J}$ and (complex conjugate) electric field $\boldsymbol{E}^*$ is evaluated over the volume V comprising all gold surfaces; all other materials are assumed lossless and therefore do not contribute to the integral. Optical properties for Au and silicon nitride are taken from ellipsometric data of experimentally deposited films. Absorbance gain g_A is calculated as the negative gradient of the absorbance landscape $-\nabla_x A(x,\lambda)$, wherein a lower numerical aperture of 0.3 NA is used to match the conditions of the lasing experiments.

The second geometry, used to compute mechanical eigenfrequencies, modal masses, static deflection and thermal responses of the devices, consists of a silicon nitride cantilever supporting a 15 nm thick Au actuator and attached to an outer frame having 1.5 µm extent (Fig. S3b). A 130 nm thick Au lead is placed overhanging a portion of the frame. Fixed boundary conditions are placed on the outer edges of the frame and the top edge temperature of the 130 nm lead is assumed to be 300 K. A cuboid measuring (350×160×40) nm^3 is placed within the cantilever and dissipates a heat load of 50 µW, as derived from the electromagnetic power loss integral. The silicon nitride has density 2200 kg·m^{-3}, elastic modulus 200 GPa, and Poisson ratio 0.2. Eigenmode calculations are performed to determine the vibrational frequencies of the cantilever, and the computed values agree with experimentally measured results to within 5 %. We evaluate the effective (modal) mass of the 6 µm cantilever by integrating the calculated mode shape Φ as

$$m_\mathrm{eff} \equiv \frac{1}{q^2}\int \rho(r)|\Phi(r)|^2\mathrm{d}V, \tag{S2}$$

where q is a normalization factor representing a generalized coordinate for the cantilever displacement at the location of the embedded localized gap plasmon resonator (LGPR), and $\rho(\mathbf{r})$ is position $\mathbf{r}$ dependent material density. A modal displacement of 0.1 times the maximum displacement at the tip as determined from finite element calculations. We find a modal mass of 2.11×10^{-15} kg for the fundamental mode.

The static downward deflection of the cantilever is produced by an elevated temperature of approximately 312 K, which is calculated as the average value over the free cantilever. The maximum downward displacement is normalized by the temperature increase of $\Delta T \approx 12$ K, and the bimorph displacement gain $g_\mathrm{B} \equiv \partial x/\partial\Delta T$ is evaluated at the cuboid location. To determine the bimorph displacement gain corresponding to the thermal excitation of the fundamental mechanical mode, we compute an overlap integral between the static displacement of the cantilever generated by the average temperature elevation of 12 K (50 pm K^{-1} at the LGPR location) and the modal displacement of the fundamental mode (Fig. S3c), giving a final value of $g_\mathrm{B} \approx 45$ pm K^{-1}. Figure S3d shows the thermal time constant of the system, evaluated by applying the heat load as a step function at 0 s.

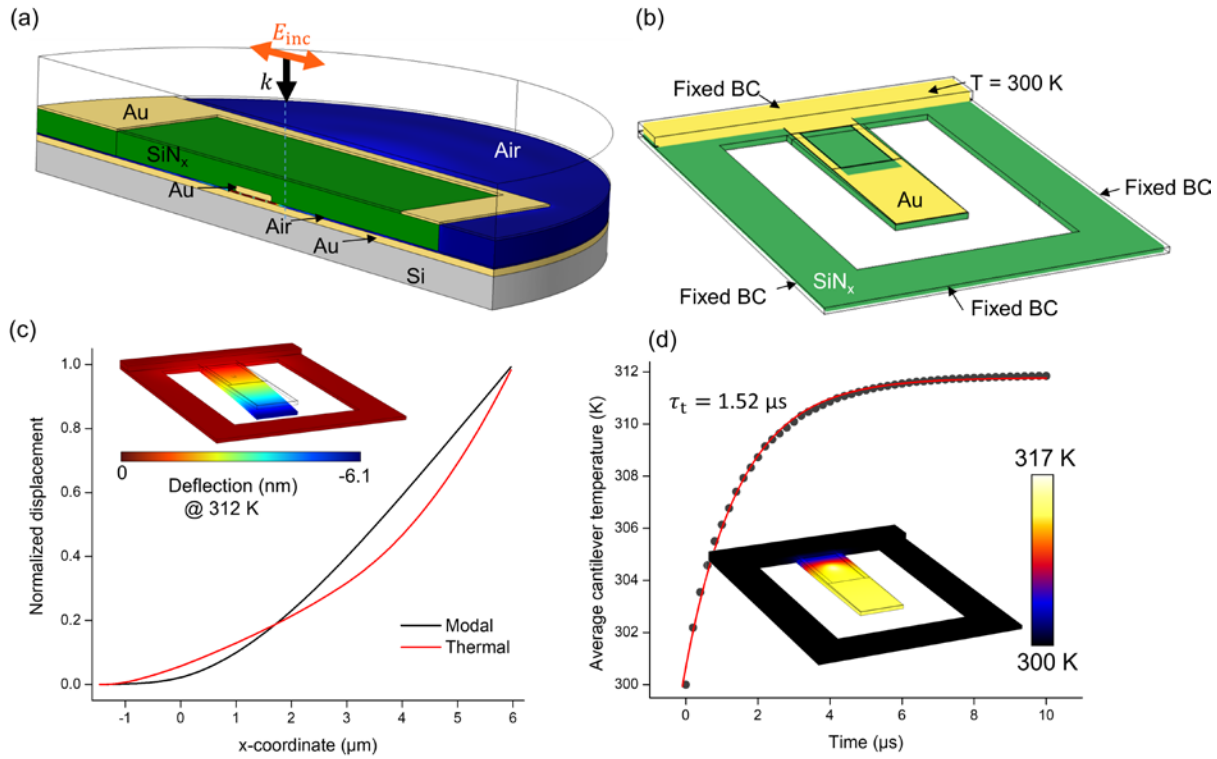

Fig. S3. Finite-element models and results. (a) Domain for electromagnetic calculations representing one half of a 4 μm length cantilever. The red arrow shows the incident electric field polarization (E_{inc}) whereas the black arrow shows the incident wavevector (k). (b) Domain for mechanical calculations. (c) Normalized absolute value of bimorph deflection (red) and modal deflection. The inset shows a 3D view of the total bimorph deflection (magnitude exaggerated) for a 50 μW heat load resulting in a 312 K average temperature. (d) Transient average temperature for the cantilever with fit to a first-order system response. Inset shows the temperature distribution of the cantilever after 10 μs of heating.

4. Intrinsic DC bias on devices

The time-varying part of the electrostatic force applied to the cantilever from the actuators is $F_{\mathrm{app}} \propto 2V_{\mathrm{DC}}V_{\mathrm{AC}} \sin \omega t + 1/2\, V_{\mathrm{AC}}^2 \sin 2\omega t$, where ω is the frequency and V_{AC} is specified voltage delivered. In our experiments, we set the offset voltage $V_{\mathrm{DC,app}}$ to zero. However, the fact that we observe device response at both ω and 2ω implies that there exists an intrinsic bias voltage in our devices $V_{\mathrm{DC}} \equiv V_{\mathrm{DC,app}} + V_{\mathrm{DC,in}} = V_{\mathrm{DC,in}}$. We determined $V_{\mathrm{DC,in}}$ by measuring the relative output voltage, as a function of input V_{AC}, on an electronic spectrum analyzer at the input frequency and second harmonic, fitting these to linear and parabolic models, respectively, and using these fit coefficients along with the expression for F_{app} to determine the relative weight of V_{DC} and V_{AC}. From this procedure, we estimate an intrinsic bias of (+0.245 $\pm$ 0.013) V, where uncertainty is derived from the voltage fits. The intrinsic DC bias is likely the result of trapped charges in the nitride from the electron-beam fabrication processing.

5. Thermal calibration in vacuum

The same transduction scheme is applied to devices placed in vacuum. In order to calibrate device thermal motion, the voltage power spectral density (PSD) is collected at low pump power ranging from 300 μW to 500 μW and fitted to Lorentzian curves, enabling extraction of the transduction gain in this

linear region of device response [S1]. We find transduction gains of (4.99 $\pm$ 0.87) mV nm^{-1} at 300 µW with a linear slope of (0.035 $\pm$ 0.0012) mV nm^{-1} µW^{-1}. Reported one standard deviation uncertainties of the transduction gain and its power-dependent slope are derived from parameter variances reported by the Lorentzian and linear fits, respectively. This linear increase in transduction gain with higher optical intensity results in a decrease of the input-referred detector dark noise and optical shot noise or equivalently, reduced imprecision noise in the motion readout. We apply linearly extrapolated calibration factors to lasing data over the full range of pump power. In order to extract the displacement, we utilize the equipartition theorem, whereby the integral of the displacement PSD corresponds to the RMS displacement of the cantilever at the location of the LGPR, i.e., $1/2\pi\int S_{xx}(\omega)d\omega \approx x_{\mathrm{eff}}^2$ [S1,S2]. Here, the effective displacement of the LGPR is given by $x_{\mathrm{eff}} = c_i x_{\mathrm{rms}}$ with average displacement $x_{\mathrm{rms}} = [k_{\mathrm{B}}T_{\mathrm{eff}}/(m_{\mathrm{eff}}\omega_{\mathrm{m}}^2)]^{1/2}$ where k_{B} is Boltzmann's constant, T_{eff} is the effective temperature, m_{eff} is the modal mass, and $c_i \approx 0.1$ is the modal displacement coefficient of the LGPR relative to the maximum tip-referenced value.

6. Control experiments

We perform two experiments to ensure that measured motion signals and self-oscillation require the presence of the LGPR. In the first we translate the probe laser from directly atop the LGPR to locations ≈ 1 µm above (toward the cantilever tip) and below (toward the base). In both experimental configurations of vacuum with 0.3 NA (Fig. S4a), and air with 0.9 NA (Fig. S4b), we observe the detected signal dropping to that background noise level upon translation of the excitation beam. Vacuum measurements correspond to transduced thermal noise of the cantilever, whereas air measurements correspond to electromechanically driven measurements of the device. In the second experiment, we rotate the input polarization of the probe laser from parallel to the LGPR long axis, which suppresses the LGP resonance (Fig. S4c), and observe the signal of the plasmomechanical oscillator (PMO) dropping abruptly to noise for polarization angles beyond approximately 30° from parallel. Further, we find that

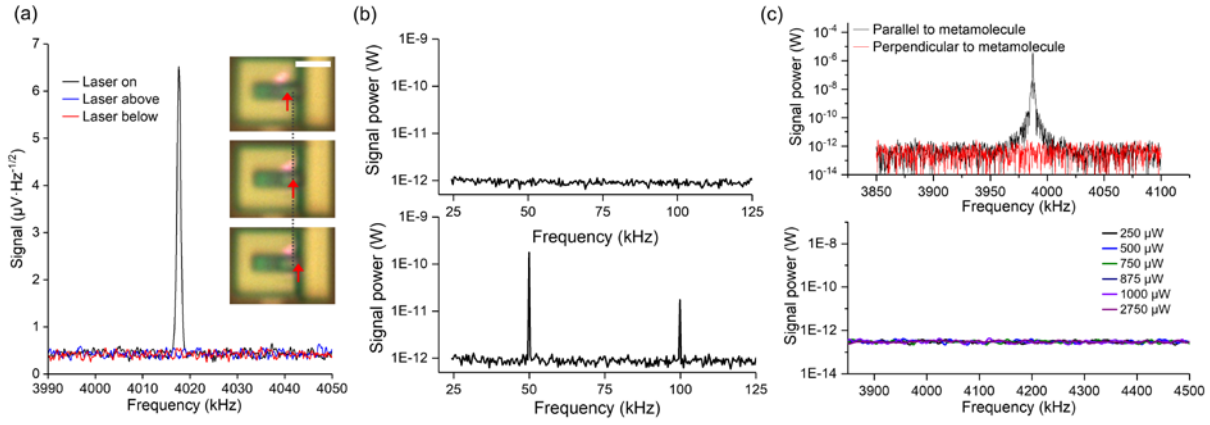

Fig. S4. Control experiments for the plasmomechanical oscillator. (a) Position dependence of thermal motion transduction in the vacuum setup with 0.3 NA objective. Inset shows optical micrographs of the ≈ 6 µm cantilever under test, with the dotted black line marking the location of the LGPR and the red arrow marking the focused beam centroid (located at approximately +1 µm, 0 um and –1 µm). The spurious light above the cantilever in the inset is due to multiple reflections in the imaging system. Scale bar is 5 µm. (b) Position dependence of driven motion detection in air (0.9 NA objective setup) with a 50 kHz drive frequency for laser positions (top panel) 1 µm above the LGPR toward the cantilever tip and (bottom panel) atop the LGPR. (c) Polarization dependence experiments showing (top panel) the PMO response with polarization parallel to the long axis of the cuboid comprising the LGPR and perpendicular; the bottom panel shows data for perpendicular polarization as a function of pump power up to the system limit of ≈ 3 mW. Data in (c) correspond to the same device as those in (a).

for perpendicular polarization, we do not observe motion transduction at any pump power up to experimental limits of 2.75 mW. These data strongly indicate that the LGPR is responsible for motion transduction and observed self-oscillation in this work [S3,S4].

As a final check to ensure that the observed optomechanical effects (modulation, transduction, and the PMO behavior) are caused by the PMO and not from the Fabry-Perot cavity formed by the nitride cantilever and underlying Au surface, we measure the reflectance of the bare nitride cantilever. Here, the spectrum of the supercontinuum laser source is first normalized to the reflection from the flat Au pad, then focused on the cantilever but displaced by ≈ 1 µm from the LGPR location. Figure S5 shows the reflectance spectrum from the cantilever (red curve) alongside the normalized spectrum collected from the Au pad (blue curve). The background reflectance $B(\lambda)$ is spectrally flat in the wavelength region from 700 nm to 850 nm and has a shallow dip near 650 nm, possibly due to the Fabry-Perot cavity amplifying the optical loss from the reduced gold reflectivity in that part of the spectrum. Given that the background spectrum is flat and experimentally indistinguishable from that of a highly reflective bare gold surface in the region where the LGP resonance occurs (from ≈ 760 nm to 820 nm), it is unlikely that a background optomechanical effect is contributing to the observed results.

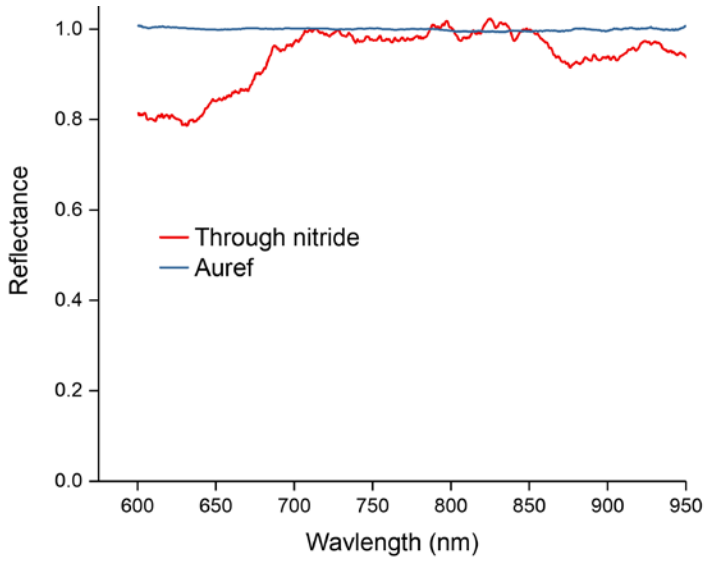

Fig. S5. Reflectance measured on the bare cantilever, displaced from the LGPR by ≈ 1 µm (red curve) alongside the reference reflectance normalized on the Au sheet (blue curve). This background reflectance is characterized by a nearly flat response between ≈ 700 nm and 850 nm and a dip near 650 nm indicating a Fabry-Perot cavity resonance between the nitride cantilever and the underlying Au pad.

7. Frequency behavior of the PMO

The plasmomechanical oscillator (PMO) exhibits rapid frequency variations at certain pump powers. While the exact nature of this rapid frequency variation is not known, it is possible to measure a stable frequency within the resolution bandwidth filter time (FWHM data in Fig. 6c inset, main text), and thus it is possible that the observed behavior derives from environmental perturbations to the setup. The ≈ 0.25 % reduction in mechanical frequency observed below threshold does not originate from an optical spring, owing to the relatively low quality factor of the LGP resonance [S5]. Whereas this minute shift may be attributed to temperature-dependent reduction in the elastic modulus of the silicon nitride, the larger frequency reduction for high pump power is likely the result of an amplitude-dependent

frequency nonlinearity occurring for strong pumping. In measuring the linewidth of the PMO (Fig. 6c in the main text), drift and vibrations in our experimental system currently make long-term measurements problematic. We therefore limit the resolution bandwidth of the ESA to 100 Hz to provide a compromise between resolution of the self-oscillation linewidth (higher resolution requiring longer sweep time) and elimination of systematic drift. Nevertheless, this measurement setting is within an order of magnitude of the expected saturation value of the linewidth of ≈ 10 Hz [S6], and the observed narrowing (broadening) of the linewidth for blue-detuned (red-detuned) pumping is consistent with expectations for our system. Furthermore, the uncertainty in the measurements is reasonably small.

8. Threshold of the PMO

Self-oscillations in the cantilevers are driven by optical-frequency dependent absorption in the plasmonic resonator. The temperature increase due to absorption causes the bimorph to expand and deflect the cantilever downward from its equilibrium position, defined in the positive x-direction. An instability occurs, owing to the reduction in absorbed optical power with increasing x resulting from the LGP resonance behavior which drives the cantilever into oscillation. The system is modeled using the following coupled equations

$$\frac{d\Delta T}{dt} = -\gamma_{\mathrm{t}}\Delta T + \frac{1}{m_{\mathrm{th}}c_{\mathrm{p}}}P_{\mathrm{abs}}(x), \tag{S3}$$

$$\frac{d^2x}{dt^2} + \gamma_{\mathrm{m}}\frac{dx}{dt} + \omega_{\mathrm{m}}^2 x = \frac{1}{m_{\mathrm{eff}}}\left[f_{\mathrm{L}} + f_{\mathrm{B}}(T) + f_{\mathrm{opt}}\right], \tag{S4}$$

where T is the device temperature, $\tau_{\mathrm{t}} = \gamma_{\mathrm{t}}^{-1}$ is the thermal time constant, $P_{\mathrm{abs}}(x)$ is the displacement-dependent optical power absorbed in the device, and $\gamma_{\mathrm{m}} = \omega_{\mathrm{m}}/Q_{\mathrm{m}}$ is the mechanical bandwidth of the cantilever with frequency ω_{m}, quality factor Q_{m}. The thermal mass m_{th}represents the full mass of the free cantilever and is ≈ 4.61×10^{-15} kg. The device is driven by the Langevin force f_{L} due to the thermal bath, the bimorph actuation force f_{B}, and the optical (radiation pressure) force $f_{\mathrm{opt}} = g_{\mathrm{om}}U/\omega_{\mathrm{LGP}}$, where U is average intracavity photon energy stored in the plasmonic resonator [S5]

$$U = \left(1 - \sqrt{R_0}\right)\frac{\gamma/2\ P_0}{\delta\omega^2 + (\gamma/2)^2}, \tag{S5}$$

where R_0 is the reflectance on resonance, $\gamma = \omega_{\mathrm{LGP}}/Q_{\mathrm{LGP}}$, P_0 is the optical power incident on the LGPR, and $\delta\omega \approx \omega - \omega_{\mathrm{LGP}}$ is the frequency detuning. Given that f_{B} derives from optical absorption in the LGPR, its magnitude is also proportional to U. However, using parameters determined below, we estimate the ratio $f_{\mathrm{B}}/f_{\mathrm{opt}} > 10^3$, indicating that radiation pressure is negligible compared to thermal backaction forces and can therefore be neglected.

To derive the threshold condition, we linearize the system around the equilibrium point $\bar{x}$ such that $x(t) = \bar{x} + x_0(t)$ for some small displacement x_0. In this limit, the change in the absorbed power and the bimorph actuation force f_{B} scale linearly with x_0 and ΔT

$$\Delta P_{\mathrm{abs}} \equiv P_0\frac{\partial\, A(\lambda,x)}{\partial x}\, x_0, \tag{S6}$$

$$f_{\mathrm{B}} \equiv m_{\mathrm{eff}}\omega_{\mathrm{m}}^2\frac{\partial x}{\partial \Delta T}\, \Delta T, \tag{S7}$$

where $A(\lambda, x)$ is the optical-wavelength and gap-size dependent absorbance of the LGP resonance, $\partial A/\partial x \equiv g_{\mathrm{A}}$ is the absorbance gain, and $\partial x/\partial \Delta T \equiv g_{\mathrm{B}}$ is the bimorph displacement gain. The system can then be recast as

$$\frac{d\Delta T}{dt} = -\gamma_{\mathrm{t}}\Delta T + \frac{P_0}{m_{\mathrm{th}}c_{\mathrm{p}}}g_{\mathrm{A}}x_0, \tag{S8}$$

$$\frac{dx_0}{dt^2} + \gamma_{\mathrm{m}} \frac{d\,x_0}{dt} + \omega_{\mathrm{m}}^2 (x_0 - g_{\mathrm{B}} \Delta T) = \frac{1}{m_{\mathrm{eff}}} f_{\mathrm{L}}. \tag{S9}$$

We note that the system described in Eq. (S8) and Eq. (S9) is the proper limit of other, more complete treatments that explicitly incorporate a third expression, describing the dynamics of the intracavity optical amplitude and coupling it to the mechanical coordinate [S7]. Under the adiabatic approximation for optical amplitude, i.e. the assumption that the thermal time τ_{t} and mechanical frequency ω_{m} are much smaller than optical cavity loss rate $\gamma_{\mathrm{LGP}} = \omega_{\mathrm{LGP}}/Q_{\mathrm{LGP}}$, the optical response follows instantaneously with the mechanical and thermal coordinates and there is negligible phase lag, therefore there is no contributions to excitation or damping from optical radiation pressure backaction. This simplification is well-justified in our experimental case, and indeed the results for the effective damping derived in our model are equivalent to those appearing elsewhere [S7,S8].

We proceed by Fourier transformation of Eq. (S8), from which we obtain the following expression for the temperature increase

$$\Delta T(\omega) = \frac{P_0}{m_{\mathrm{th}} c_{\mathrm{p}}} \frac{1}{(\gamma_{\mathrm{t}} + i\omega)}\, g_{\mathrm{A}} x_0, \tag{S10}$$

where ω is the Fourier frequency. Applying Fourier transformation to Eq. (S9), using Eq. (S10), and collecting imaginary terms, we find the effective damping coefficient

$$\gamma_{\mathrm{eff}} = \gamma_{\mathrm{m}} + \omega_{\mathrm{m}}^2 \frac{P_0}{m_{\mathrm{th}} c_{\mathrm{p}}} \frac{g_{\mathrm{A}} g_{\mathrm{B}}}{\omega^2 + \gamma_{\mathrm{t}}^2}, \tag{S11}$$

where the second term describes the contribution of the photothermal spring to the overall system damping. Threshold is crossed when γ_{eff} passes through zero and becomes negative, which requires that $g_{\mathrm{A}} < 0$, leading to the expression for threshold power at the mechanical resonance $\omega = \omega_{\mathrm{m}}$

$$P_{\mathrm{thresh}} = \frac{m_{\mathrm{th}}\, c_{\mathrm{p}}}{|g_{\mathrm{A}}| g_{\mathrm{B}}} \frac{\omega_{\mathrm{m}}^2 + \gamma_{\mathrm{t}}^2}{Q_{\mathrm{m}} \omega_{\mathrm{m}}}. \tag{S12}$$

As shown in Fig. 7 in the main text, the condition $g_{\mathrm{A}} < 0$ is met both for blue-detuned dispersive devices as well as reactive devices with any detuning. This unique feature enables self-oscillation for a wide variety of device configurations.

9. Sonification of the injection-locked PMO

We have performed sonification [S9] of real-time injection locking data from one of our devices (Fig. S6, Supplement 2). We used a ≈ 6 μm device with ≈ 19 pm (100 mV) injection amplitude. The horizontal axis frequencies in Fig. S6 were mapped to the audible range from approximately 200 Hz to 40000 Hz. We provide a string of 188 segments taken from a continuous voltage trace during the locking experiment. Each sequential segment is ≈ 0.25 s in length, spaced equidistantly, and normalized in amplitude. The key features of the locking experiment are evident from the audio file. The initially free-running MPL is evident as the strong tone with frequency of ≈ 3 kHz at the beginning of the audio. The injected frequency, the MPL, and the generated sidebands are audible at an initial frequency of ≈ 200 Hz and increase in pitch until approximately 16 s into the audio. At this point, the signal abruptly changes to a nearly pure tone which increases in pitch with time, signifying locking. The data in Fig. S6 contains a stitch between two contiguous frequency sweeps at an injection frequency of ≈ 4300 kHz, resulting from a spurious electronic signal, which produces an audible distortion near 22 s in the audio trace.

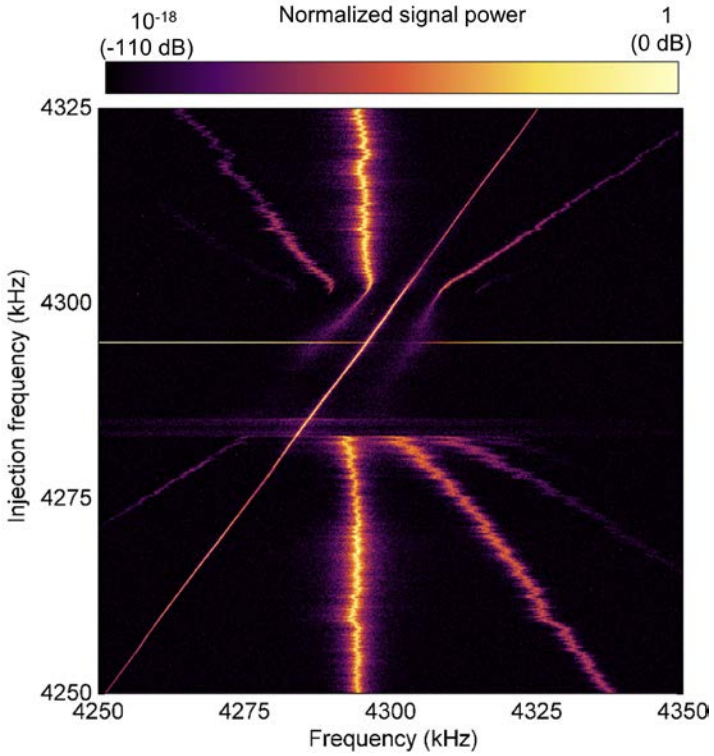

Fig. S6. Injection locking data for sonification. Contour plot of injection locking of a 6 µm cantilever device using 19 pm (100 mV) injection amplitude. The injection frequency sweep is from the bottom left ≈ 4250 kHz to the top right ≈ 4325 kHz, occurring over ≈ 48 s. The stitch in the data occurring at 4290 kHz is due to a spurious signal and is not representative of injection locking dynamics.

10. Injection locking at increased injection amplitudes

Figure S7 shows a suite of injection locking data for increasing injection amplitudes from ≈ 10 pm to ≈ 48 pm mechanical amplitudes. The injection amplitude corresponds to the calibrated value of the RF tone peak measured far from the PMO free running frequency. Several key features are evident as the injected amplitude increase. First, the locking range increases with an approximate square-root dependence. Second, the distortion sidebands and the frequency pulling outside the locking range increase. Finally, within the locking range, a larger number of nonlinear sidebands – those not described by linear locking theory – are observed. The exact nature of the sidebands is not known, but they may originate from optical transduction nonlinearities or from mechanical nonlinearities induced at high injection amplitude.

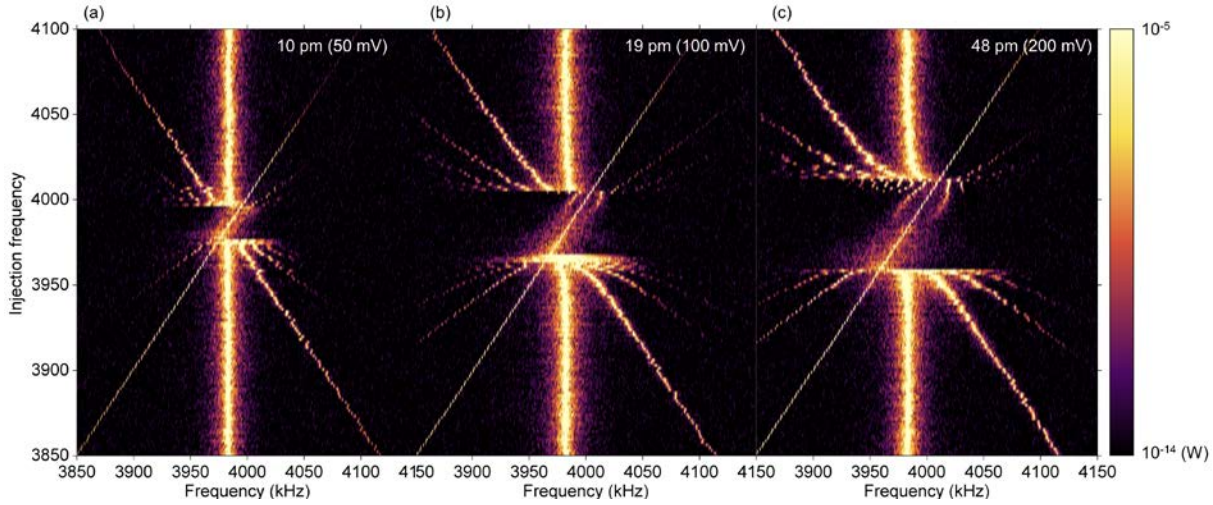

Fig. S7. Injection locking at various injection amplitudes of (a) 10 pm, (b) 19 pm, and (c) 48 pm.

References

S1. B. D. Hauer, C. Doolin, K. S. D. Beach, and J. P. Davis, "A general procedure for thermomechanical calibration of nano/micro-mechanical resonators," Ann. Phys. **339**, 181–207 (2013).

S2. C. Metzger and K. Karrai, "Cavity cooling of a microlever," Nature **432**, 1002–1005 (2004).

S3. R. Thijssen, T. J. Kippenberg, A. Polman, and E. Verhagen, "Plasmomechanical resonators based on dimer nanoantennas," Nano Lett. **15**, 3971–3976 (2015).

S4. B. J. Roxworthy and V. A. Aksyuk, "Nanomechanical motion transduction with a scalable localized gap plasmon architecture," Nat. Commun. **7**, 13746 (2016).

S5. M. Aspelmeyer, T. J. Kippenberg, and F. Marquardt, "Cavity optomechanics," Rev. Mod. Phys. **86**, 1391–1452 (2014).

S6. J. B. Khurgin, M. W. Pruessner, T. H. Stievater, and W. S. Rabinovich, "Laser-rate-equation description of optomechanical oscillators," Phys. Rev. Lett. **108**, 223904 (2012).

S7. H. Zhu, F. Yi, and E. Cubukcu, "Plasmonic metamaterial absorber for broadband manipulation of mechanical resonances," Nat. Photonics **10**, 709–714 (2016).

S8. S. Zaitsev, A. K. Pandey, O. Shtempluck, and E. Buks, "Forced and self-excited oscillations of an optomechanical cavity," Phys. Rev. E **84**, 046605 (2011).

S9. W. L. Diaz-Merced, R. M. Candey, N. Brickhouse, M. Schneps, J. C. Mannone, S. Brewster, and K. Kolenberg, "Sonification of astronomical data," Proc. Int. Astron. Union **7**, 133–136 (2011).